Remote Sensing of Environment 313 (2024) 114376

Contents lists available at ScienceDirect

Remote Sensing of Environment

journal homepage: www.elsevier.com/locate/rse

Increase in gross primary production of boreal forests balanced out by increase in ecosystem respiration

Jouni Pulliainen [a,*], Mika Aurela [a], Tuula Aalto [a], Kristin Böttcher [b], Juval Cohen [a], Chris Derksen [c], Martin Heimann [d], Manuel Helbig [e,f], Pasi Kolari [g], Anna Kontu [a], Alisa Krasnova [h,i], Samuli Launiainen [j], Juha Lemmetyinen [a], Hannakaisa Lindqvist [a], Anders Lindroth [k], Annalea Lohila [a,g], Kari Luojus [a], Ivan Mammarella [g], Tiina Markkanen [a], Elma Nevala [a], Steffen Noe [h], Matthias Peichl [i], Jukka Pumpanen [l], Kimmo Rautiainen [a], Miia Salminen [a], Oliver Sonnentag [f], Matias Takala [a], Tea Thum [a], Timo Vesala [g], Patrik Vestin [k]

[a] Finnish Meteorological Institute, P.O. Box 503, FI-00101 Helsinki, Finland
[b] Finnish Environment Institute, Latokartanonkaari 11, FI-00790 Helsinki, Finland
[c] Climate Research Division, Environment and Climate Change Canada, Ontario M3H 5T4, Canada
[d] Max-Planck-Institute for Biogeochemistry, PF 100164, D-07701 Jena, Germany
[e] Dalhousie University, NS, B3H 4R2 Halifax, Canada
[f] Université de Montréal, Quebec H2V 2B8, Canada
[g] University of Helsinki, P.O. Box 68, FI-00014 University of Helsinki, Finland
[h] Estonian University of Life Sciences, Kreutzwaldi 1, EE-51006 Tartu, Estonia
[i] Swedish University of Agricultural Sciences, SE-90183 Umeå, Sweden
[j] Natural Resources Institute Finland, FI-00790 Helsinki, Finland
[k] Lund University, SE-22362 Lund, Sweden
[l] University of Eastern Finland, P.O. Box 1627, FI-70211 Kuopio, Finland

ARTICLE INFO

Editor: Jing M. Chen

Keywords:
Remote sensing of boreal forests
Remote sensing of cryosphere
Carbon balance
Net carbon sink
Eddy covariance
Passive microwave remote sensing

ABSTRACT

Changes in the net carbon sink of boreal forests constitute a major source of uncertainty in the future global carbon budget and, hence, climate change projections. The annual net ecosystem exchange of carbon dioxide (CO_2) controlling the terrestrial carbon stock results from the small difference between respiratory CO_2 release and the photosynthetic CO_2 uptake by vegetation. The boreal forest, and the boreal biome in general, is regarded as a persistent and even increasing net carbon sink. However, decreases in photosynthetic CO_2 uptake and/or concurrent increases in respiratory CO_2 release under a changing climate may turn boreal forests from a net sink to a net source of CO_2. Here, we assessed the interannual variability of the boreal forest net CO_2 sink-source strength and its two component fluxes from 1981 to 2018. Our remote sensing approach - trained by net CO_2 flux observations at eddy covariance sites across the circumpolar boreal forests - employs satellite-derived retrievals of snowmelt timing, landscape freeze-thaw status, and yearly maximum estimates of the normalized difference vegetation index as a proxy for peak vegetation productivity. Our results suggest that for the period 2000–2018, the mean annual evergreen boreal forest CO_2 photosynthetic uptake (gross primary productivity) was 2.8±0.2 Pg C y^{-1} (1.6±0.1 Pg C y^{-1} for Eurasia and 1.2±0.1 Pg C y^{-1} for North America). In contrast to earlier studies results obtained here do not indicate a clear increasing trend in the circumpolar evergreen boreal forest CO_2 sink. The increase in photosynthetic CO_2 uptake is compensated by increasing respiratory releases with both component fluxes showing considerable interannual variabilities.

* Corresponding author.
E-mail address: jouni.pulliainen@fmi.fi (J. Pulliainen).

https://doi.org/10.1016/j.rse.2024.114376
Received 25 February 2024; Received in revised form 14 August 2024; Accepted 18 August 2024
Available online 24 August 2024

1. Introduction

1.1. Background and objective

Boreal forests comprise one of the largest terrestrial carbon stocks on Earth, even though reported estimates on its magnitude vary considerably from 367 to 1716 Pg (Bradshaw and Warkentin, 2015). Unlike tropical forests, the bulk of the boreal forest carbon is stored belowground (Pan et al., 2011; Bradshaw and Warkentin, 2015). Earlier studies have suggested a persistent increase of the boreal forest and the whole boreal region carbon stock along with increasing trends in the carbon sink strength across both Eurasia and North America (Pan et al., 2011; Sitch et al., 2015; Friedlingstein et al., 2022; Yang et al., 2023). However, the boreal forest may change from a net carbon sink to a net carbon source in response to a warming climate, altered precipitation patterns, and intensifying disturbance regimes (Bradshaw and Warkentin, 2015; Foster et al., 2022).

Excluding disturbances (e.g., forest fires) the annual net ecosystem carbon dioxide (CO_2) exchange (NEE) is the small difference between annually integrated ecosystem respiration (ER) and photosynthetic carbon dioxide uptake (gross primary production, GPP) (Chapin et al., 2006). The CO_2 uptake of evergreen boreal forests through photosynthesis starts in spring with increasing day length and air temperature (Tanja et al., 2003) and is also affected by the timing of snow melt and the thawing of underlying frozen soil which provides access to liquid water for root uptake (Frolking et al., 1996; Rautiainen et al., 2014; Pulliainen et al., 2017). Photosynthetic CO_2 uptake reaches its maximum during the summer months (June to August) and gradually ceases in fall with diminishing day length and decreasing air temperature (Hollinger et al., 1999; Launiainen et al., 2022). Thus, annual NEE across the boreal biome is influenced by the length of the photosynthetically active period, which in turn, is affected by landscape freeze-thaw status (Suni et al., 2003; Thum et al., 2009; Randazzo et al., 2021; El-Amine et al., 2022). Earlier spring thaw and delayed onset of autumn freeze-up have contrasting effects on the annual carbon balance of boreal forests (Piao et al., 2008; Richardson et al., 2010; Pulliainen et al., 2017). Delayed autumn freeze-up increases the annual ER (releases of CO_2 to the atmosphere are higher under thawed conditions), whereas earlier spring snow-melt and soil thaw increase the annual CO_2 uptake.

Observations from space-borne microwave radiometers allow detection of landscape freeze-thaw status as well as snow accumulation and melt (Takala et al., 2009; Kim et al., 2011; Pulliainen et al., 2020). Microwave radiometers offer a way to estimate the spring recovery of photosynthesis through the timing of snow-melt (Pulliainen et al., 2017), and they enable detecting changes in ER through the timing of landscape freezing and thawing. How these translate to changes in (mean) annual GPP, ER and NEE has remained unknown. Satellite-based snow cover and landscape freeze-thaw data products derived from passive microwave radiometry are available with close to daily global coverage starting from the late 1970s, providing the possibility to investigate intra- and inter-annual variability and trends of GPP and ER over multiple decades (Kim et al., 2017; Luojus et al., 2021).

Supplemented by optical satellite data of vegetation greenness, we here utilize multi-decadal time series of passive microwave data products on snow cover and landscape freeze-thaw status to obtain estimates on the changes in mean annual ER, and GPP, and thus NEE of circumpolar boreal forests. The hypothesis is that freeze-thaw estimates based on microwave data, supported by optical satellite data-derived spectral vegetation indices, can provide approximations of annual ER, GPP and NEE estimates independent of terrestrial biosphere models. The Normalized Difference Vegetation Index (NDVI) is used here as a proxy of vegetation productivity, since the global time series is available starting from 1981 from the Advanced Very High Resolution Radiometer (AVHRR) observations (Vermote et al., 2018).

The approach developed here provides estimates of the annual carbon exchange of circumpolar evergreen boreal forests from 1981 to 2018 by combining snow and landscape freeze-thaw satellite products with daily CO_2 flux estimates measured with the eddy covariance technique (Table 1) (Kim et al., 2017; Vermote et al., 2018; Pulliainen et al., 2020; Luojus et al., 2021; Pulliainen et al., 2021; Pallandt et al., 2022). Combining satellite information on seasonal dynamics governing ecosystem processes with annual CO_2 flux estimates over evergreen boreal forests (derived from tower-based eddy covariance measurements available since 1990s), proxies for the mean annual GPP, ER and NEE can be constructed for a multi-decadal period using statistical analysis. Cryosphere information from passive microwave satellite radiometry, supported by vegetation information from optical satellite spectrometry, has not previously been used to investigate annual NEE, GPP or ER.

1.2. Limitations of current carbon exchange assessments

Current estimates of the annual net CO_2 sink-source strength across the circumpolar evergreen boreal forest, utilizing terrestrial biosphere models including data assimilation, are subject to high uncertainties. They suggest that the boreal forest is likely a net carbon sink, but possibly a net carbon source (Bradshaw and Warkentin, 2015; Sitch et al., 2015; López-Blanco et al., 2019; Virkkala et al., 2021; Yang et al., 2023). One source of uncertainties is the lack of reliable estimates of the belowground carbon stock and its role in ecosystem respiration (López-Blanco et al., 2019). The sparseness of in situ observation networks including eddy covariance flux measurements (Pallandt et al., 2022) is another major source of uncertainty highlighting the need for remote sensing and modelling approaches – or their combination – to assess the regional CO_2 balance. Prognostic terrestrial biosphere models enable the simulation of past, present, and future CO_2 exchanges (Fisher et al., 2018). However, intercomparisons of terrestrial biosphere models have indicated large uncertainties at the regional scale owing to the discrepancies among models (Huntzinger et al., 2012; Fisher et al., 2018). The evaluation of modelling approaches and model-based trend analyses requires comparisons with independent multi-decadal time series of CO_2 balance and component fluxes.

A recent multi-source data assimilation investigation by López-Blanco et al. (2019) using a terrestrial biosphere model DALEC2 indicated a boreal forest CO_2 sink for the period 2000–2015 with the median annual NEE of -110 g C m^{-2} y^{-1} with 90% confidence ranging from -388 to 1196 g C m^{-2} y^{-1}, i.e., from a moderate net carbon sink (indicated by the minus sign) to a large source (López-Blanco et al., 2019). Their estimated median annual GPP was 760 g C $m^{-2}y^{-1}$ with a 90% confidence range from 584 to 968 g C m^{-2} y^{-1}. For the annual ER, they reported nearly order of magnitude uncertainty, a 90% confidence range from 285 to 2114 g C m^{-2} y^{-1} (median 635 g C m^{-2} y^{-1}).

Investigations using only satellite data are typically limited to GPP or net primary production based on observations across optical wavelengths, e.g., using vegetation indices or estimates of solar-induced vegetation fluorescence (Xiao et al., 2019). Recently, approaches estimating global GPP by applying vegetation optical depth from passive radiometer or active radar microwave observations have been introduced (Teubner et al., 2019; Wild et al., 2022). Distributed eddy covariance CO_2 flux observations have been used together with optical-range satellite observations from sensors such as the Moderate Resolution Imaging Spectroradiometer (MODIS), to quantify GPP, ER and NEE. In practice, satellite MODIS data-derived vegetation indices or reflectances are used as input to light use efficiency models, machine learning or regression algorithms (Ryu et al., 2019; Xiao et al., 2019). For example, results for North America covering the period 2001–2012 showed moderate magnitudes of mean annual GPP and ER for the forest regions of Canada and the northern parts of the conterminous U.S., ~800–1200 and ~ 600–800 g C m^{-2} y^{-1}, respectively (Xiao et al., 2014). For Canadian forests and U.S. Rocky Mountains, NEE ranged from ~ − 100 to ~ − 200 g C m^{-2} y^{-1}, whereas the strongest net CO_2

Table 1
Characteristics of flux sites and flux dataset[a].

	Country (lat, lon)	Years of flux obs.[b]	Forest, climate & frost zone	Tree species	Tree age[c] (years)	Soil type	Number of freeze days[b,d] (min/ med/max)	Max. daily GPP/ ER[e] ($gCm^{-2}d^{-1}$)
CAN SMC (Sonnentag, 2021)	Canada (N63.15, W123.25)	2018	Northern boreal, discont. Permafrost	Black spruce	–	Peat soil	171/171/ 171	10.2/6.7
CAN HPC (Sonnentag and Marsh, 2021)	Canada (N68.32, W133.52)	2013, 2017, 2018	Northern boreal, cont. Permafrost	Black spruce	–	–	176/196/ 243	10.8/7.2
CAN SCC (Helbig et al., 2017)	Canada (N61.31, W121.30)	2015–2018	Northern boreal, sporadic permafrost	Black spruce	–	Mineral and peat soil	152/ 167.5/175	6.5/5.8
BERMS OBS (Barr et al., 2009)	Canada (N53.99, W105.12)	2000–2011	Southern boreal, seasonal soil frost	(old) Black spruce	120	Mineral and peat soil	123/147/ 202	9.3/9.8
BERMS OJP (Barr et al., 2009)	Canada (N53.92, W104.69)	2000–2011	Southern boreal, seasonal soil frost	(old) Jack pine	70	Mineral soil	111/143/ 184	7.6/7.6
Estonia tower 2 (Krasnova et al., 2022)	Estonia (N58.28, E27.31)	2017	Hemiboreal, seasonal soil frost	Birch, aspen, Scots pine	–	Mineral soil	81/81/81	19.0/18.4
Estonia tower 1 (Krasnova et al.,2022)	Estonia (N58.28, E27.31)	2017	Hemiboreal, seasonal soil frost	Scots pine	–	Mineral soil	81/81/81	18.3/13.3
Estonia tower A (Krasnova et al., 2022)	Estonia (N58.27, E27.27)	2015–2018	Hemiboreal, seasonal soil frost	Norway spruce, birch	70	Mineral soil	76/79/87	26.8/33.3
Zotino (Lloyd et al., 2002)	Russia (N60.80, E89.35)	2002–2004	Northern boreal, seasonal soil frost	Scots pine	up to 200	Mineral soil	194/197/ 201	8.9/5.9
Fyodorovskoye (Milyukova et al., 2002)	Russia (N56.46, E32.92)	1999–2009	Southern boreal, seasonal soil frost	Norway spruce	150	Mineral-peat soil	62/117/ 129	17.9/16.7
Svartberget (Chi et al., 2021)	Sweden (N64.26, E19.78)	2015–2016, 2018	Northern boreal, seasonal soil frost	Scots pine, Norway spruce	110	Mineral soil	141/147/ 158	9.9/13.0
Rosinedal (Jocher et al., 2017)	Sweden (N64.17, E19.74)	2015–2018	Northern boreal, seasonal soil frost	Scots pine	90	Mineral soil	107/148.5/162	6.6./9.7
Norunda[f] (Lagergren et al., 2008; Vestin et al., 2020)	Sweden (N60.09, E17.48)	1995–2002, 2007–2008	Southern boreal, seasonal soil frost	Norway spruce, Scots pine, clear-cut	60–110 0	Mineral soil	23/89/162	16.3/17.7
Kenttärova (Aurela et al., 2015)	Finland (N67.98, E24.25)	2003–2013	Northern boreal, seasonal soil frost	Norway spruce	70–160	Mineral soil	151/184/ 195	8.1/5.8
Sodankylä (Thum et al., 2009)	Finland (N67.37, E26.63)	2001–2016	Northern boreal, seasonal soil frost	Scots pine	80–180	Mineral soil	121/174.5/196	8.8/10.1
Hyytiälä (Lagergren et al., 2008; Thum et al., 2009)	Finland (N61.85, E24.28)	2001–2018	Southern boreal, seasonal soil frost	Scots pine	40–50	Mineral soil	42/117.5/196	12.9/8.9

[a] Flux data and their processing procedures are described in reference listed in the table.
[b] Years with daily flux observations.
[c] During the flux data acquisition period.
[d] Based on satellite observations of cryosphere status.
[e] Based on daily flux dataset.
[f] Includes two clear-cut sites with EC flux towers in addition to coniferous forest flux site.

sink was estimated for both the eastern U.S. and the Pacific Coast (mean annual NEE from ~ -300 to ~ -600 g C m^{-2} y^{-1}). Small magnitudes of mean annual GPP and ER were indicated for Alaska and northern Canada (< 500 g C m^{-2} y^{-1}). However, annual CO_2 emissions from wildfires may exceed the magnitude of mean annual NEE in North American boreal forests resulting in forests being a carbon source (Zhao et al., 2021). In this study, we broaden the suite of approaches on a hemispheric scale by utilizing long time series of passive microwave data-derived landscape freeze-thaw status information, NDVI and flux-tower data from boreal forests.

2. Material and methods

2.1. Generation of the circumpolar and flux station datasets

Snow and landscape freeze-thaw information was obtained by fusing two datasets, the GlobSnow v3.0 climate data record (CDR) (Pulliainen et al., 2020; Luojus et al., 2021), and the landscape freeze-thaw Earth system data record (FT-ESDR) (Kim et al., 2011; Kim et al., 2017). Both products (starting from 1979) are based on the global space-borne microwave radiometer data time series from a sensor suite including the Scanning Multichannel Microwave Radiometer (SMMR) and several succeeding Special Sensor Microwave/Imager instruments (SSM/I and SSMIS sensors). The FT-ESDR product indicates the landscape freeze-thaw status for each satellite data pixel throughout the year (Kim

et al., 2017), whereas the GlobSnow data record provides a daily estimate of the snow water equivalent for each satellite data pixel with the exact timing of snow clearance estimated from the radiometer data time series using a change detection algorithm (Pulliainen, 2006; Takala et al., 2009; Takala et al., 2011; Luojus et al., 2021).

The two radiometer products were combined on a fixed equal-area terrestrial grid (EASE Grid of 625 km^2 grid cells), with one of five different daily landscape status values determined for each grid cell: (a) thawed snow-free, (b) frozen snow-free, (c) thawed soil during fall with (dry) snow cover, (d) frozen soil with dry snow cover and (e) melting snow cover (soil frozen or top-soil thawed) (Pulliainen et al., 2021). For the analyses here, this classification was simplified to two classes: (1) thawed conditions (class a) and (2) frozen soil and/or snow cover (classes b, c, d, e). In practice, the freezing of the landscape in autumn was determined through the FT-ESDR product and the timing of snow clearance and the concurrent estimate for soil thawing was obtained by the GlobSnow product as the latter considers snow clearance accurately for boreal forests (Takala et al., 2009). Additionally, the summer maximum Normalized Difference Vegetation Index (NDVI) was extracted for evergreen forested areas of each investigated EASE Grid cell from the AVHRR NDVI data at 0.05° spatial resolution (Vermote et al., 2018). In practice, the maximum NDVI for the period 20 June - 31 July, corresponding to annual peak GPP period, was extracted from ca. 25 AVHRR pixels covering each EASE Grid cell considering pixels with a forest coverage fraction higher than 50%.

All satellite datasets were rectified to the same EASE Grid of 625 km^2 grid cells, and annual lengths of freeze-thaw conditions were calculated for all grid cells that represent the circumpolar evergreen boreal forest. The forested pixels included into the analysis were selected using a criterion that the grid cell must have at least a 30% fraction of conifer evergreen forest (larch-dominated Siberian forests are excluded). The analysis based on the ESA GlobCover and ESA Climate Change Initiative Land Cover dataset (Bontemps et al., 2011). Additionally, we restricted to grid cells for which at least 80% of winters have over 59 snow days during the first half of the year based on the GlobSnow CDR, which makes the investigated forested area slightly smaller than in previous studies (Pulliainen et al., 2017). The total forested area investigated here comprises 2.05 10^6 km^2 forests in Eurasia, and 1.52 10^6 km^2 in North America, respectively (Table 2).

The eddy covariance (EC) flux station dataset includes gap-filled daily averaged net CO_2 fluxes from 16 circumpolar sites (Pallandt et al., 2022) that predominantly include mature forest stands (Table 1). The flux stations in Canada, Estonia, Finland, Russia and Sweden provide altogether 114 site years of NEE from which GPP and ER were partitioned using established methods (Lasslop et al., 2012). The gap-filling and partitioning methods varied depending upon which network an individual station belongs (Table 1). The set of 16 stations was supplemented by two clear-cut sites in Norunda, Sweden, with two-year-long time series of flux observations and NDVI information of a high spatial resolution extracted from Landsat data (Vestin et al., 2020). The clear-cut sites co-locate in the same EaseGrid cell as the Norunda's spruce and pine-dominated station. Mean annual values of NEE, GPP and ER [gC m^{-2} y^{-1}] were calculated for all 116 flux observation time series. The flux dataset extends from 1995 to 2018 and they were compared with the coinciding satellite data-based freeze-thaw and NDVI information from the overlapping grid cell.

Additional independent data for the comparison with the flux station data and our satellite-based estimate include NEE, GPP and ER estimates from FLUXCOM product (Jung et al., 2020), JSBACH simulations (Reick et al., 2013) driven by CRU-JRA dataset (Harris and Osborn, 2014), and TRENDY DLEM-S3 simulations (Tian et al., 2015). The FLUXCOM record provides time series of NEE, GPP and ER retrieved by applying machine learning techniques to eddy covariance flux tower, meteorological, climate and optical remote sensing (MODIS) data (Jung et al., 2020). JSBACH model was applied to provide carbon cycle-climate predictions similar to TRENDY simulations using CRU-JRA data (Harris and Osborn, 2014) for the meteorological forcing (however, without using dynamic land cover characteristics). The third dataset for comparison is the DLEM-S3 simulation that is one of the TRENDY datasets (Friedlingstein et al., 2022).

Further benchmarking of our new GPP estimates was carried out using the MODIS GPP product (Running and Zhao, 2021), and the employed peak NDVI values were compared with summer maximum values of solar-induced fluorescences (SIF) obtained from the merged Global Ozone Monitoring Experiment 2 (GOME-2) and Sentinel-5P TROPOMI satellite observations (Duveiller et al., 2020; Guanter et al., 2021).

Table 2
Mean annual ecosystem CO_2 fluxes[a] for 2000–2018.

Area	Flux [g C m^{-2} y^{-1}]	2000-2018[b]
Evergreen boreal forests of Northern Hemisphere (3.5702 10^6 km^2)	GPP	795 ± 60
	ER	741 ± 60
	NEE[c]	-55 ± 84
Eurasia (2.0538 10^6 km^2)	GPP	794 ± 60
	ER	741 ± 60
	NEE[c]	−53 ± 84
North America (1.5164 10^6 km^2)	GPP	797 ± 60
	ER	740 ± 60
	NEE[c]	−57 ± 84
Area	**Flux [Pg C y^{-1}]**	**2000-2018[a]**
Evergreen boreal forests of Northern Hemisphere (3.5702 10^6 km^2)	GPP	2.8 ± 0.2
	ER	2.6 ± 0.2
	NEE[c]	−0.2 ± 0.3
Eurasia (2.0538 10^6 km^2)	GPP	1.6 ± 0.1
	ER	1.5 ± 0.2
	NEE[c]	−0.1 ± 0.2
North America (1.5164 10^6 km^2)	GPP	1.2 ± 0.1
	ER	1.1 ± 0.1
	NEE[c]	−0.1 ± 0.1

[a] Estimates by the linear model for mean annual GPP (**Eq.1**) and exponential model for mean annual ER (**Eq.3**).
[b] Error bounds (±std) are obtained by boostrap analysis. The error bound value across the investigated period is the average of different years due to the non-zero covariance of interannual errrors.
[c] NEE is obtained from the difference between the spatially averaged values of GPP and ER (negative values of mean annual NEE indicate a net sink of CO_2).

2.2. Predicting NEE, GPP and ER by satellite data

The analysis of the coinciding satellite and flux station data set indicated that the summer maximum NDVI and the lengths of the annual or first half of year thaw seasons, and especially their product, are strongly correlated with the cumulative GPP and ER for the respective period (Figs. 1, 2, **Table S1**). The evident reasons for the observed correlation include that the length of thaw season is connected (a) to the timing of the spring recovery of photosystem II activity with temperatures raising above the freezing point (Ensminger et al., 2004), and (b) to the reduction of liquid water, required for biological activity, due to the freezing of soil in autumn (El-Amine et al., 2022). Additionally, liquid water from thawed soil is needed for full photosynthetic recovery in spring to supply water to trees (Kimball et al., 2004; Monson et al., 2005; Barr et al., 2009; El-Amine et al., 2022). During thaw, also the decomposition of organic matter strongly increases (Goulden et al., 1998). Moreover, the end of growing season, as observed from GPP, could be explained at boreal spruce forests by the decrease of soil liquid water content and the formation of the seasonal snow pack (El-Amine et al., 2022).

Thus, we can approximate the mean annual GPP (ER) with a two-dimensional linear model:

$$z = f(x,y) + \varepsilon = \beta_1 xy + \beta_0 + \varepsilon \quad (1)$$

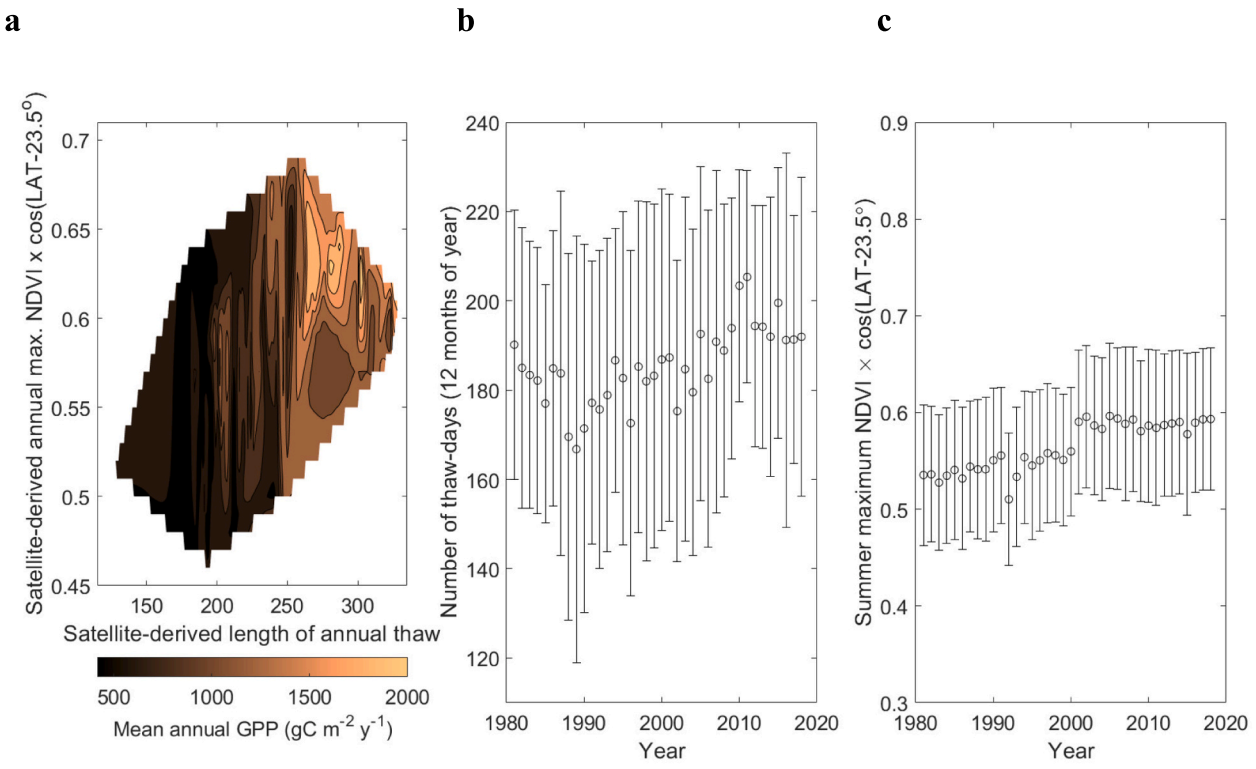

Fig. 1. Flux station data derived GPP and the drivers of the developed satellite proxy (**Eq.**1). Both GPP and ER are driven by the product of summer maximum NDVI with the latitude correction and the length of annual thaw. The two-dimensional response of the mean annual GPP to the two driver variables is interpolated from flux station data-derived GPP **(a)**. The range of interannual variabilility of driver variables across the circumpolar boreal forests, depicted by circles and standard deviation bars **(b-c)**, is captured by the range of conditions in the applied flux observation data set **(a)**.

where.z = mean annual GPP (ER) [g C m−2 y−1].x = length of thaw, i.e., the number of thawed, snow-free days during a single year or first half of the year based on satellite data.y = $NDVI_{max}cos(LAT - 23.5^{\circ})$, where $NDVI_{max}$ is the annual maximum value for the grid cell (EASE Grid) from AVHRR data and LAT is the latitude (the correction approximately considers the decrese of incoming light due to Earth's curvature).ε = random error [g C m−2 y−1].

For estimating GPP [g C m^{-2} y^{-1}], by linear regression the obtained regression coefficient values were $\beta_0 = -314.3$ and $\beta_1 = 9.859$ (Fig. 3**)**. However, the dataset used for training regression algorithms (Fig. 2) suggests that an exponential relationship between mean annual ER and the length of annual thaw provides a better agreement than a linear approach. Thus, in addition to (Eq.1), we apply a regression formula to describe the logarithmic value of ER:

$$ln\left(ER/1\mathrm{gCm^{-2}y^{-1}}\right) = ln(z) = g(x,y) + \varepsilon' = \beta'_1 xy + \beta'_0 + \varepsilon' \quad (2)$$

When x = length of annual thaw and y = $NDVI_{max}cos(LAT - 23.5^{\circ})$ in Eq.2, we get the regression coefficient values β'_0 and β'_1 by fitting the product x•y to the logarithmic value of ER resulting in $\beta'_0 = 5.4615$ and $\beta'_1 = 0.0095$.

Eq.2 leads to:

$$ER = exp\left(\beta'_1 xy + \beta'_0 + \varepsilon'\right) \bullet 1\ \mathrm{gCm^{-2}y^{-1}}. \quad (3)$$

Parameters β_0 and β_1 in **Eq.**1, and β'_0 and β'_1 in **Eqs.** 2 and 3, are determined through linear regression by analysing satellite data-derived product *xy* against each of the 114 mean annual values of GPP (ER) from EC flux stations, i.e., by least-squares fitting the formula to the training dataset including 114 flux data-based mean annual values of GPP and 108 mean annual values of ER (hemiboreal Estonian forests were ecluded in the training of the algorithm), see Fig. 2. The highest performance in estimating GPP and ER is obtained by using the length of the annual thaw (in *x*) and latitudinal correction for $NDVI_{max}$ in *y* (linear model (**Eq.**1) for GPP and exponential model (**Eq.**3) for ER).

To establish an ensemble of model predictions for GPP, we also applied a model with the length of six-month spring thaw as a predictor variable, and for ER predictions by both the linear and exponential models were considered. As an outcome, model combinations according to Fig. 2, indicating a significant correlation between the satellite data derived freeze-thaw and NDVI conditions, were included in the analysis to provide a proxy for GPP and ER. Thus, GPP was predicted with two models and ER with four models.

For the mapping of circumpolar values of mean annual GPP and ER we applied (**Eqs.**1 and 3) to all grid cells representing evergreen boreal forests. Circumpolar, North American, and European scale estimates of mean annual NEE were determined by subtracting the regional average of GPP from the regional value of mean annual ER. As two models were used for GPP and four models for ER (Fig. 2), the estimates of NEE were obtained with eight combinations, which enables a consideration of uncertainties associated to the overall analysis. Circumpolar/continental scale averages and statistical error bounds of annual GPP, ER and NEE estimates were determined through a bootstrap analysis. The bootstrap algorithms (**Eqs.**1 and 3) were trained by taking 10,000 resamples with replacement from the training data set divided to ten clusters of nearby or individual flux stations (nine clusters excluding Estonian stations in the case of ER). Flux stations (Table 1) from four regions were grouped together in the analysis since the number of observation years was small for individual stations (Estonia, northern Sweden, Russia, and Northwest Canada). The bootstrap analysis enables the estimation of ±1 std. (standard deviation) error bounds from the set of obtained 10,000 algorithms.

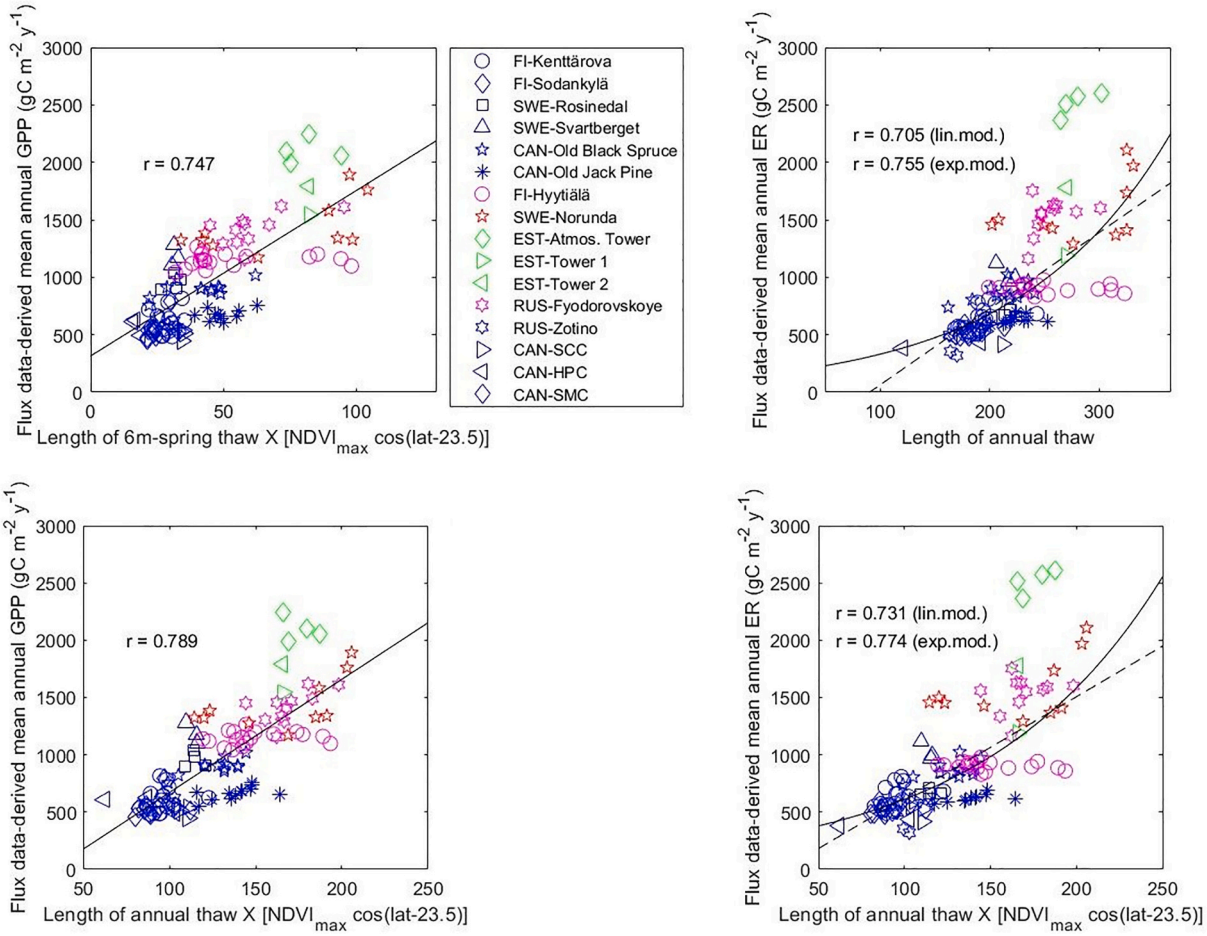

Fig. 2. Relationship between the drivers of the proxy (latitudinally corrected NDVI and length of annual or six-month spring thaw) and flux station data-derived GPP and ER (mean annual values and maximum values of daily means for each year). The model fitting according to (**Eqs.**1 and 3) are also shown.

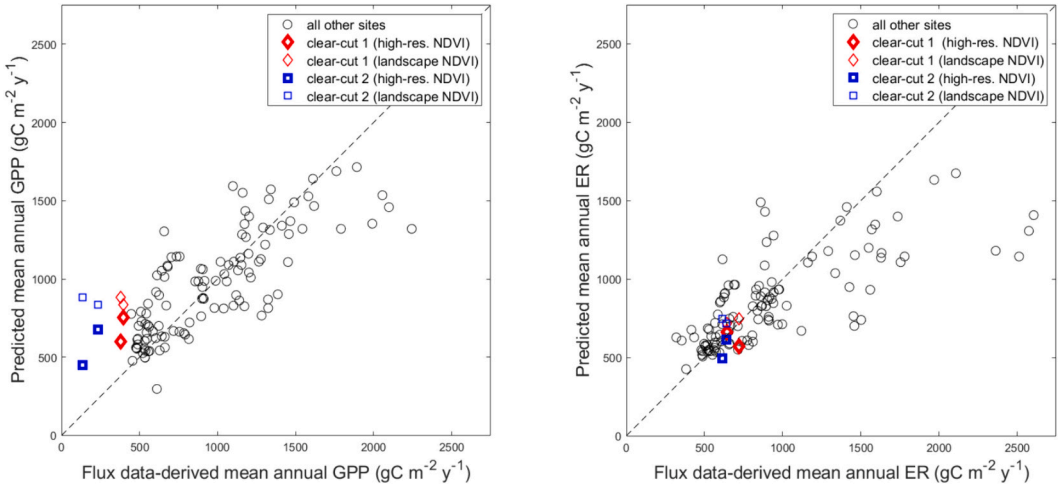

Fig. 3. Performances of linear regression (**Eq.**1) and exponential (**Eq.**3) algorithms for predicting mean annual GPP and ER, respectively, at CO_2 flux stations used for training the algorithms. The product of space-borne observed annual length of thaw and latitude factor corrected summer maximum landscape scale NDVI is used as a predictor variable. Algorithms are also tested for small clear-cut test sites that are not included in the training data set by applying a landscape scale value of NDVI and site-specific NDVI observed at a high spatial resolution.

3. Results and discussion

3.1. Methodology assessment

Excluding the small clear-cut areas, the overall coefficient of determination (R^2) of the algorithm using the global landscape scale NDVI information as input was 0.62 for GPP and 0.55 for ER, respectively, when testing included the hemiboreal Estonian stations (Fig. 3). The results of Fig. 3 are obtained by the baseline algorithm (**Eqs.1 and 3**) using the the length of annual thaw and latitudinally corrected NDVI as the predictor variable. The comparison of daily flux data with the satellite data-derived daily freeze-thaw status of landscape indicates that the overall behavior of GPP and ER is strongly correlated with changes in freeze-thaw conditions, and further, a significant correlation exists between the thawed-season GPP (ER) and the latitude-corrected summer maximum NDVI (**Fig. S1**). The results of bootstrap analysis indicate only a small bias both for the mean annual GPP (6.0 g C m^{-2} y^{-1}) and ER (−30.3 g C m^{-2} y^{-1}), which suggests that our spatially distributed estimates have only a small systematic error (Fig. 4).

The same predictor variable, i.e., the product of annual thaw length and $NDVI_{max}$, was used as a baseline for both GPP and ER since it provided the highest correlation between the satellite observations and the flux data-derived mean annual values of GPP and ER. However, all models shown in Fig. 2 were included to obtain an ensemble of model predictions for the period from 1981 to 2018. They apply different predictor variables, e.g., length of snow cover during the first half of the year, in addition to the length of annual thaw, for predicting GPP. Thus, the estimated temporal dynamics of GPP and ER varies within the ensemble as different drivers are used in the predictor variable. This also facilitates an additional uncertainty analysis of the predicted time series and trends of GPP, ER and NEE. Since NEE is the small difference between ER and GPP - and random error in estimating ER and GPP is relatively high and correlated - the spatial pattern of NEE cannot be reliably estimated for small regions (for continental-scale random estimation error is averaged out, which was confirmed by investigating the systematic error through a bootstrap testing).

The validity of the developed approach was further investigated by analysing the temporal behavior of NEE, GPP and ER estimation error at the locations of circumpolar flux towers (Figs. 5, 6). The difference between flux data-derived values and satellite estimates indicates that for both Eurasia and North America the overall bias does not show any significant trend during the period of flux observations (Fig. 6). Further, the bias of NEE estimates by the satellite proxy compared with EC records for 1995–2018 does not show any trend, and only small trends for the other investigated data records (FLUXCOM, JSBACH, DLEM-S3). Instead, the biases with respect to flux station-observed NEE show analogous interannual fluctuations, and the mean values by satellite proxy, JSBACH, FLUXCOM and DLEM-S3 are close to each other for all years (Fig. 5a). Flux data on NEE, incorporating multiple stations, is available for the period 1999–2018 (for Norunda, Sweden, also for 1995–1998). Since the available set of reporting flux stations varies from year to year (Table 1), the biases also vary interannually (Fig. 5a).

The comparison of the developed satellite proxy at the flux site locations indicates a relatively good agreement with the MODIS GPP product (Running and Zhao, 2021) ($R^2 = 0.69$, Fig. 7). Compared with the in situ measured EC fluxes, the MODIS product appears to underestimate annual GPP for values above 1200 g C m^{-2} y^{-1} (nevertheless, the overall correlation is high ($R^2 = 0.69$)). Additionally, the comparison of the employed summer maximum NDVI with the summer maximum value of solar-induced chlorophyll fluorescence (SIF) obtained from a merged time series of GOME-2 and TROPOMI satellite observations (Duveiller et al., 2020; Guanter et al., 2021) indicates that the NDVI information is highly correlated with the magnitude of boreal forest vegetation photosynthesis (Fig. 8). Thus, the summer maximum NDVI explains well the spatio-temporal variability of peak vegetation productivity. Additionally, the latitudinally corrected peak NDVI is correlated with both the flux data-derived mean daily summertime GPP and ER (**Fig. S1**). Since NDVI is a band difference ratio, it is a robust index for generating long time series despite its limitations, e.g., saturation for dense vegetation canopies (Jiang et al., 2008). Some other indices, such as the Chlorophyll Carotenoid Index (CCI) (Gamon et al., 2016) may provide better accuracies for estimating GPP in boreal forests, but CCI can be only calculated from MODIS satellite data for shorter periods. Time series of NIRv index can be calculated from AVHRR observations, but a study by Pierrat et al. (2022) suggests that NIRv does not improve the relationship with GPP (on a monthly time scale) in comparison with NDVI for boreal forests.

Growing season length can be also estimated by using vegetation indices derived from optical-range satellite data. However, photosynthetic activity in boreal evergreen forest begins before changes in green biomass, thus there is a delay of several weeks between photosynthetic recovery and increase of greenness as observed from vegetation indices (such as NDVI and EVI) (Melaas et al., 2013; Walther et al., 2016; Pierrat et al., 2021; Melser et al., 2024). The application of vegetation indices

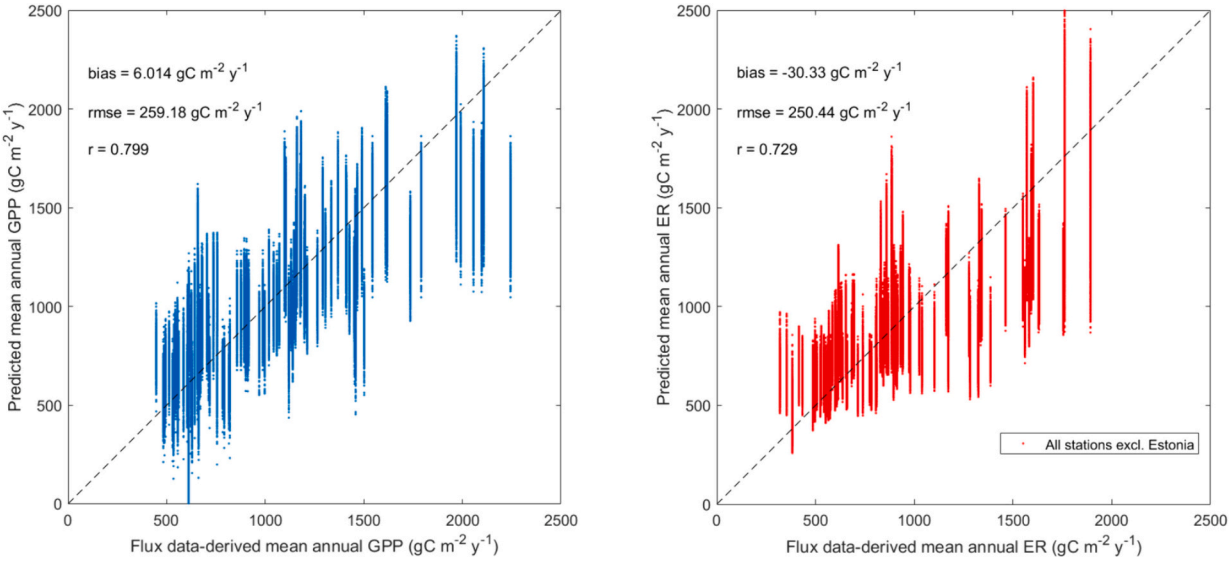

Fig. 4. Regression algorithm performance in the estimation of mean annual GPP and ER from passive microwave radiometry and NDVI data (linear approach for GPP and exponential approach for ER corresponding to Fig. 3). Bootstrap regression analysis is used for determining the error bounds of GPP and ER estimates.

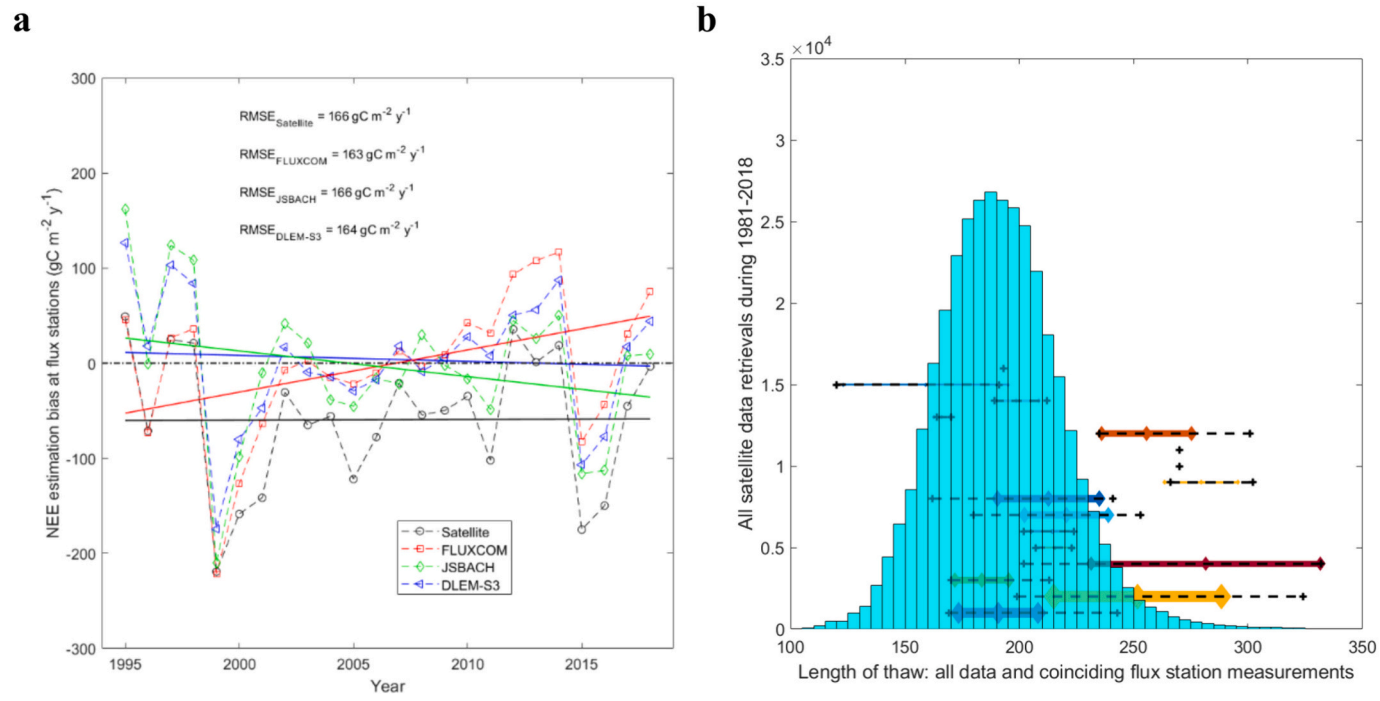

Fig. 5. Comparison of satellite-derived mean annual NEE with flux site observations and freeze-thaw conditions in the flux data set vs. conditions in the satellite dataset. **a**, Bias of mean annual NEE estimates is compared with flux station NEE observations (averages for all reporting stations for different years); solid lines show the fitted trends of biases for the estimates by satellite proxy, FLUXCOM, JSBACH and DLEM-S3; NEE estimation error root mean squared values are calculated for all 114 observation cases. **b**, Comparison of the length of thaw at all flux stations with all satellite observations across 1981–2018, the thickness of horizontal bars indicate the number of flux observations per station with diamonds indicating the average ± std., and plus signs indicating maximum and minimum values.

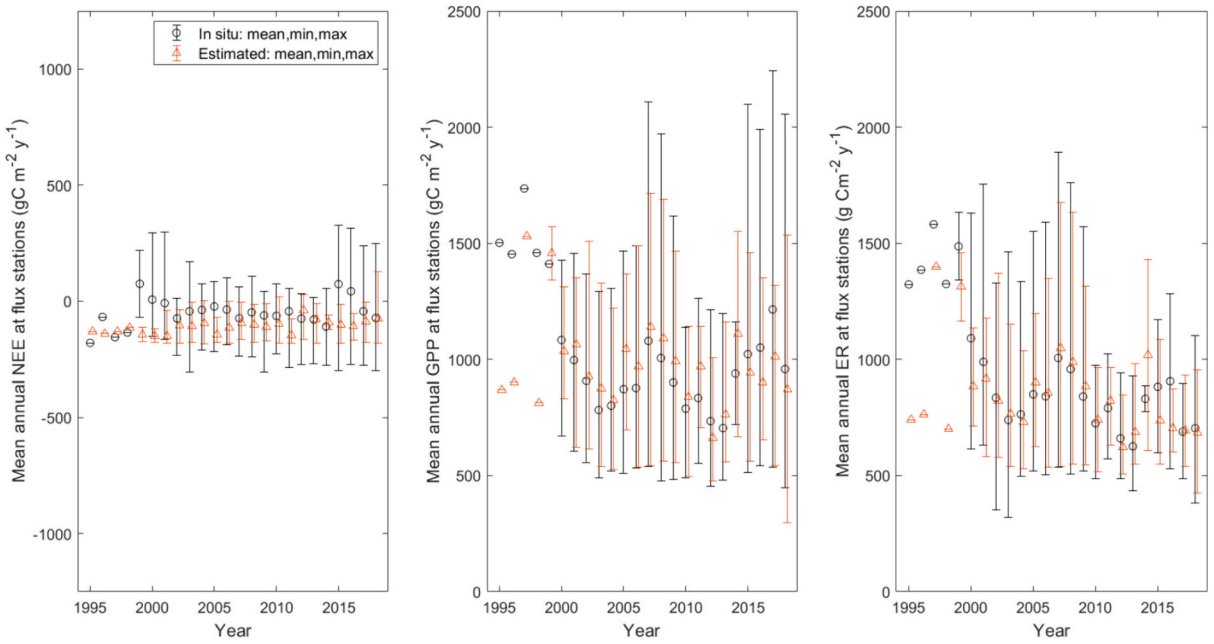

Fig. 6. Comparison of satellite-derived mean annual NEE, GPP and ER with those based on the eddy-covariance dataValues for different stations, excluding hemiboreal forests in Estonia, are shown for each year (for 1995–1998 daily CO_2 flux observations are only available for Norunda, Sweden).

from optical instruments in autumn in the boreal region is challenging, due to reduced sun light at the high latitudes. Furthermore, photosynthesis can continue in evergreen forest until the occurrence of severe frost (Vogg et al., 1998).

3.2. *Refined carbon exchange estimates*

We predicted the mean annual GPP and ER from the product of thaw period length and summer maximum NDVI for each grid cell representing the evergreen boreal forest by using **Eqs.1** and **3** (Fig. 9). The GPP was estimated with two approaches (annual thaw length or first half of year thaw length in the predictor) and ER was estimated with four

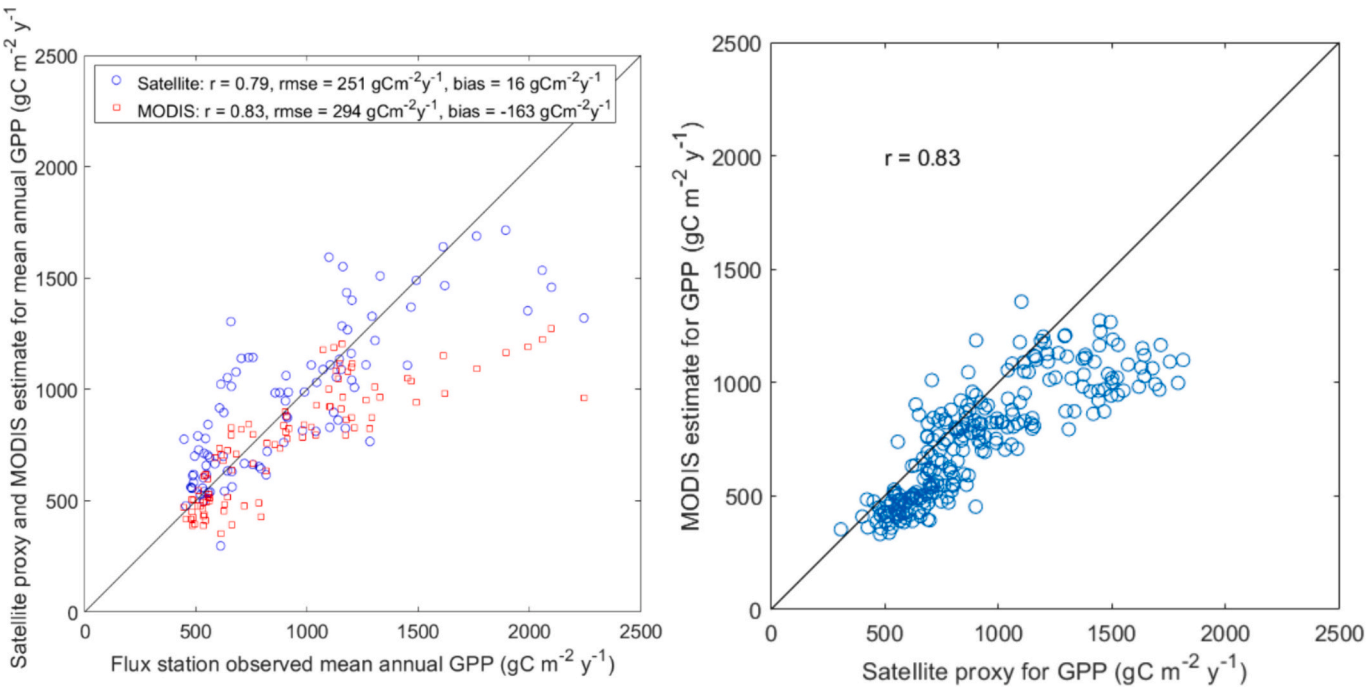

Fig. 7. Comparison of satellite proxy and MODIS GPP. Left: MODIS GPP and satellite proxy against flux data-derived mean annual GPP. Right: Comparison of estimated mean annual values of GPP at the locations of the employed circumpolar flux stations from 2002 to 2018. The MODIS GPP is based on observations by Aqua and Terra satellites (Running and Zhao, 2021). (For interpretation of the references to colour in this figure legend, the reader is referred to the web version of this article.)

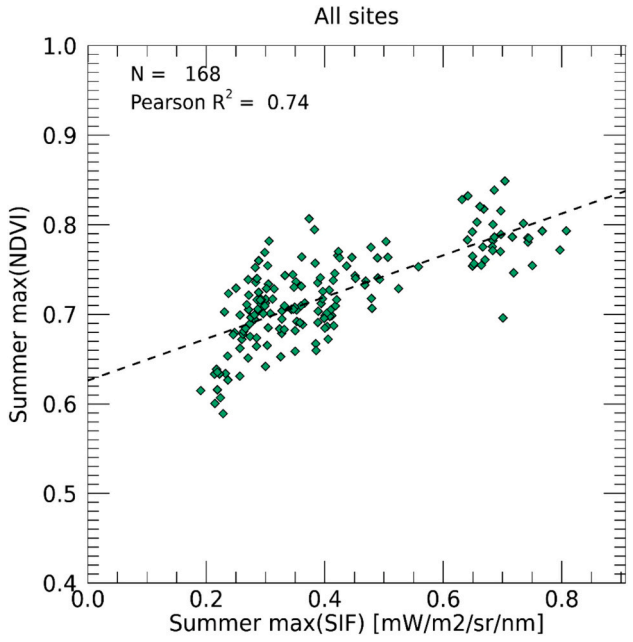

Fig. 8. Comparison of AVHRR NDVI and downscaled merged GOME-2 and TROPOMI SIF for 2007–2018. The summer maximum SIF at flux stations is compared with the summer maximum NDVI used in GPP and ER algorithms to consider the strength of photosynthesis of evergreen boreal forests of each investigated EASE Grid cell.

approaches (Fig. 2). Circumpolar mean annual GPP and ER were calculated by averaging all estimates of forested grid cells for each year. NEE was estimated by subtracting the circumpolar annual GPP from the corresponding spatially averaged ER. Thus, NEE was predicted by eight combinations, arising from GPP and ER models. The depicted annual averages and their error bounds (Fig. 9) were determined through the bootstrap analysis (the statistical accuracy bounds are only shown for the baseline model that gives the highest performance). The increasing circumpolar trends of mean annual GPP and ER during the period 1981–2018 are statistically significant ($p < 0.05$) for all model variants obtained by the bootstrap analysis. The exponential model (**Eq.3**) was used as a baseline to estimate the mean annual ER. The results by using six-month spring thaw in the predictor variable for GPP yield substantially higher values than those with the length of annual thaw in the predictor (even though the correlation between these two thaw lengths is high, **Fig. S2**). This leads to shifted estimates of mean annual NEE for the period from 1981 to 1999 (Fig. 9a). The difference between the linear and exponential approaches for ER further indicates the uncertainty of the obtained estimates.

Our satellite-derived GPP shows a substantial decrease with increasing latitude (Fig. 10). Additionally, the temporal variability of circumpolar mean annual GPP and ER is high (Fig. 9b, c). The variability is, however, dampened in NEE (Fig. 9a), but the relative uncertainty of NEE estimates is much higher since NEE is the small difference between two relatively large component fluxes, i.e., mean annual ER and GPP. There has been a positive trend in GPP and ER during the period 1990–2011, but no significant trends thereafter (Fig. 9b, c). Both variables are the lowest during the 1980s and early 1990s. Also, the net carbon sink strength is the weakest for the 1980s and early 1990s, or forests may have been even a carbon source (Fig. 9a). The obtained estimates of mean annual NEE at the circumpolar scale indicate a possible slight increase of carbon sink strength (Fig. 9). This increase is driven largely by the GPP increase that started in early 1990s and continued until 2011. However, within the period 2012–2018 the circumpolar evergreen boreal forest carbon sink strength does not show any trend. Both the estimated GPP and ER dropped to constant levels after the peak values in 2010 and 2011 (Fig. 9). Table 2 summarizes the hemispheric and continental scale estimates of GPP, ER and NEE for the period 2000–2018. These values with their uncertainties are obtained by the baseline model that uses the length of annual thaw as a driver of the

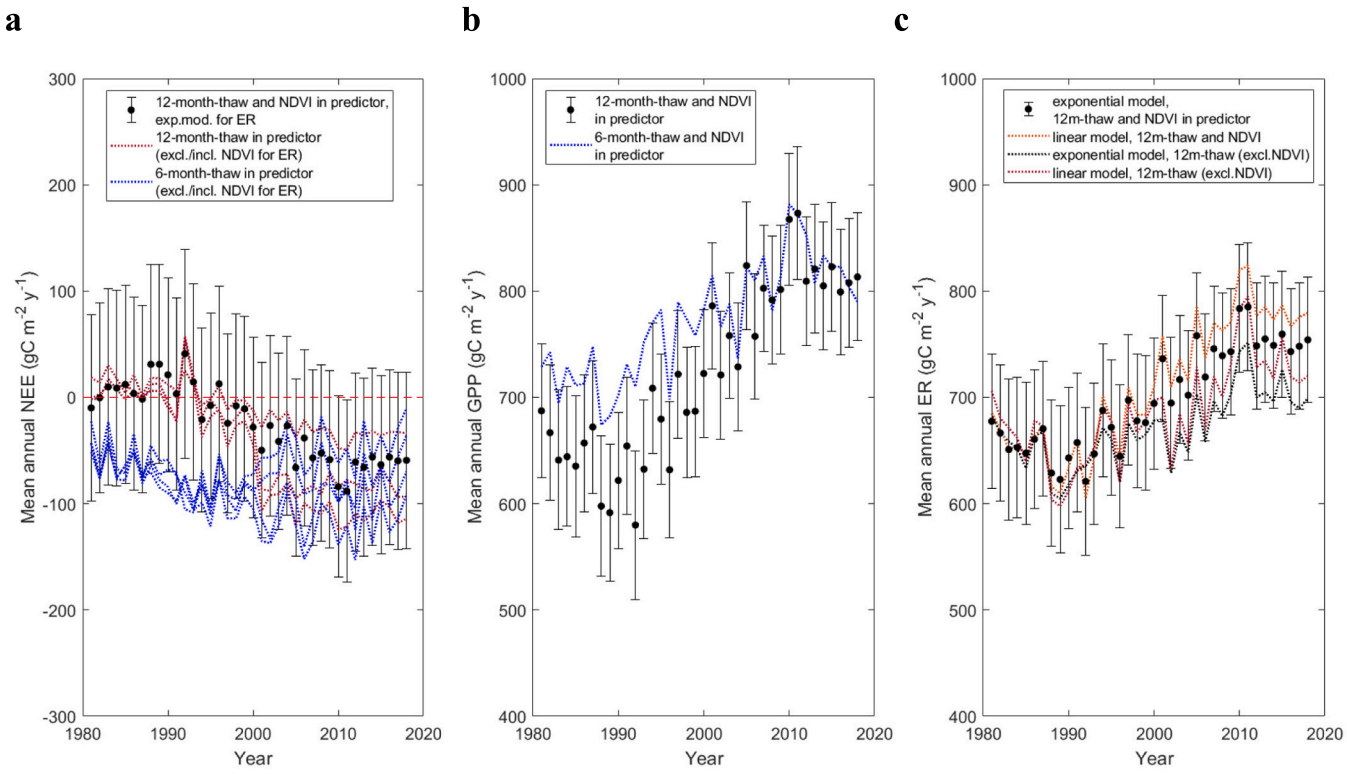

Fig. 9. Time series of mean annual GPP, ER and NEE (g C m^{-2} y^{-1}) using the ensemble approach of driver combinations. Annual estimates are obtained using the developed satellite proxy (**Eqs.**1 and 3) for the circumpolar evergreen boreal forest. NEE is the difference between the circumpolar average ER and GPP (note that NEE is negative for a net carbon sink). Black circles depict the estimates obtained by the logarithmic model of mean annual ER (**Eq.**3). For this baseline approach ±1 std. uncertainty bounds from the bootstrap analysis are also shown. The ±1 std. uncertainty bounds for the exponential ER model are close to those of the linear model.

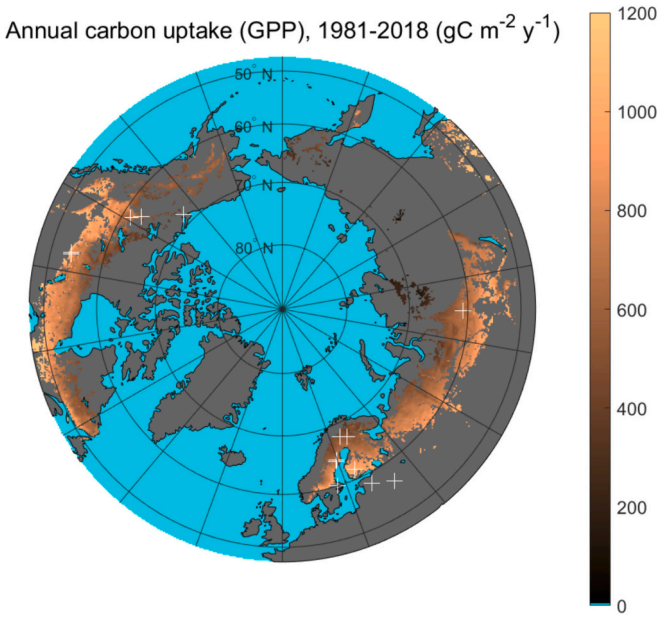

Fig. 10. Estimated mean annual GPP of evergreen boreal forests across the period 1981–2018. The spatial distribution of the average level of mean annual GPP across the investigated period is depicted. Red crosses show the locations of the employed eddy covariance CO_2 flux measurement stations. (For interpretation of the references to colour in this figure legend, the reader is referred to the web version of this article.)

proxy (both GPP and ER) and the exponential approach for ER (**Eq.**3). Quantitative estimates for the period 1981–1999 are not shown in Table 2, since the spread in ensemble predictions of GPP and NEE is high for that period.

The dynamic drivers of GPP and ER proxies are the satellite-derived length of the annual or six-month spring thaw and the annual maximum NDVI. Flux data-derived GPP and ER can be described as a two-dimensional function (product) of these drivers (Fig. 1a), since the results suggest that the maximum annual NDVI is related to the level of summer maximum photosynthesis (Fig. 8) and the length of annual thaw is related to the length of the photosynthetically active period (Fig. 1a). Decrease in the length of annual thaw from 1981 to 1989 (Fig. 1b) results in a small decrease of estimated GPP and ER during that period (Figs. 9b, c). A progression of longer thaw seasons extends from 1990 through 2011, with little change between 2012 and 2018 (Fig. 1b). Increasing length of annual thaw resulted in the multi-decadal growth in GPP and ER, followed by a lack of increase after 2011 (Figs. 1b, 9b, c). Maximum summertime NDVI affects more the spatial pattern of GPP and ER than the temporal variability (Figs. 1c, 10).

Inter-annual variability and trends in our novel satellite-based NEE, GPP and ER estimates are predominantly driven by changes in thaw length (Figs. 1, 9). Even though the available flux data do not extend to earlier years, the drivers of the developed satellite proxy suggests a small decrease in GPP and ER through 1981–1990 (note that the variablity of thaw length at flux data is similar to the variability of freeze-thaw conditions within the evergreen boreal forest zone across 1981–2018 (Fig. 5b)). The pixel-wise median effect of annual (12-month) thaw length variability to the estimated mean annual GPP is 580 g C m^{-2} y^{-1} during the period of 38 years, whereas the median dynamic effect of the latitudinally corrected NDVI driver is 279 g C m^{-2} y^{-1}.

Even though CO_2 releases to the atmosphere by disturbances are not

considered, the developed approach indirectly considers the effects of harvesting, forest fires and other land cover changes to GPP and ER as the summer maximum NDVI is used as a multiplier within the predictor variable of the developed regression algorithm. Maximum NDVI incorporates the influence of interannual changes in forest vegetation peak photosynthesis, which is a factor also related to interannual land cover changes. To show this, we tested the algorithm for two clear-cut sites by applying NDVI information obtained at a high spatial resolution for these sites, Fig. 3 (Vestin et al., 2020). The results showed that the regression algorithm captured better the mean annual GPP and ER when NDVI information specific to clear-cut sites was applied instead of landscape scale values of NDVI (landscape scale values are virtually not affected by individual small scale land cover changes). Thus, we can conclude that the algorithm takes into account the reduction of GPP and ER caused by the shrinking of forest photosynthesis due to changes in forest cover within the grid cell under investigation.

3.3. Comparison with other approaches

We compared our novel method with three established approaches, the JSBACH terrestrial biosphere model (Reick et al., 2013), the FLUXCOM record (Jung et al., 2020) and the TRENDY DLEM-S3 product (Friedlingstein et al., 2022; Tian et al., 2015). The JSBACH simulation provided a multi-decadal temporal evolution in GPP and ER comparable to that of our analysis, even though the mean levels are lower (Fig. 11). The underestimation of mean annual ER is a common feature of terrestrial biosphere models owing to high uncertainty in the simulation of unfrozen sub-surface soil during autumn and early/deep winter (Byrne et al., 2022). The FLUXCOM time series does not show any trend in NEE across the evergreen boreal zone through the investigated period but the magnitude of NEE is similar to our estimates, although our analysis indicates a weak increasing trend in the carbon sink strength for the years 1993–2012. For 2010–2018 the circumpolar average NEE by FLUXCOM, JSBACH and by our analysis show a good agreement. However, both FLUXCOM and JSBACH suggest generally lower levels of GPP and ER compared to our estimates. Comparison of DLEM-S3 model simulations and FLUXCOM data with Eurasian and North American flux observations employed here show a smaller spatio-temporal variability compared to our estimates and the in situ flux data (Fig. 11**, Fig. S3**). For the 1981–2018 period, the spatial variability of of both GPP and ER in our satellite-based estimate and FLUXCOM are well comparable (**Fig. S4**).

4. Summary and conclusions

We developed a novel method to estimate the trends of mean annual net ecosystem CO_2 exchange of evergreen boreal forests by using passive microwave and optical satellite data, including cryosphere information based on passive microwave observations. The analysis here focused on evergreen boreal forests excluding larch-dominated forest areas. Obtained estimates of annual CO_2 uptake (GPP) and ecosystem respiration (ER) provide new insight into the drivers, magnitudes, and trends of boreal carbon exchange and, thus, the net CO_2 sink-source strength for the period 1981–2018. The conducted analysis for boreal forest eddy covariance flux stations indicates that the product of satellite-derived annual thaw length and summer maximum NDVI is highly correlated with the mean annual values of GPP and ER. We compared our results with independent approaches. However, any conclusions on absolute accuracies of different data sets cannot be made beyond the comparisons made with the employed flux station data set (Fig. 5, Fig. 7, Fig. 11, **Fig. S3**, **Fig. S4**). Moreover, earlier investigations also indicate high uncertainties in the assessment of annual balances (López-Blanco et al., 2019).

Our analysis suggests interannual and decadal variabilities both in GPP and ER that are not evident in earlier predictions of evergreen boreal forest CO_2 sink-source strength (Figs. 9b, c, 11b, c). Our results show that the evergreen boreal forest of the Northern Hemisphere is a weak net CO_2 sink (-55 ± 84 g C m^{-2} y^{-1} for 2000–2018), even though

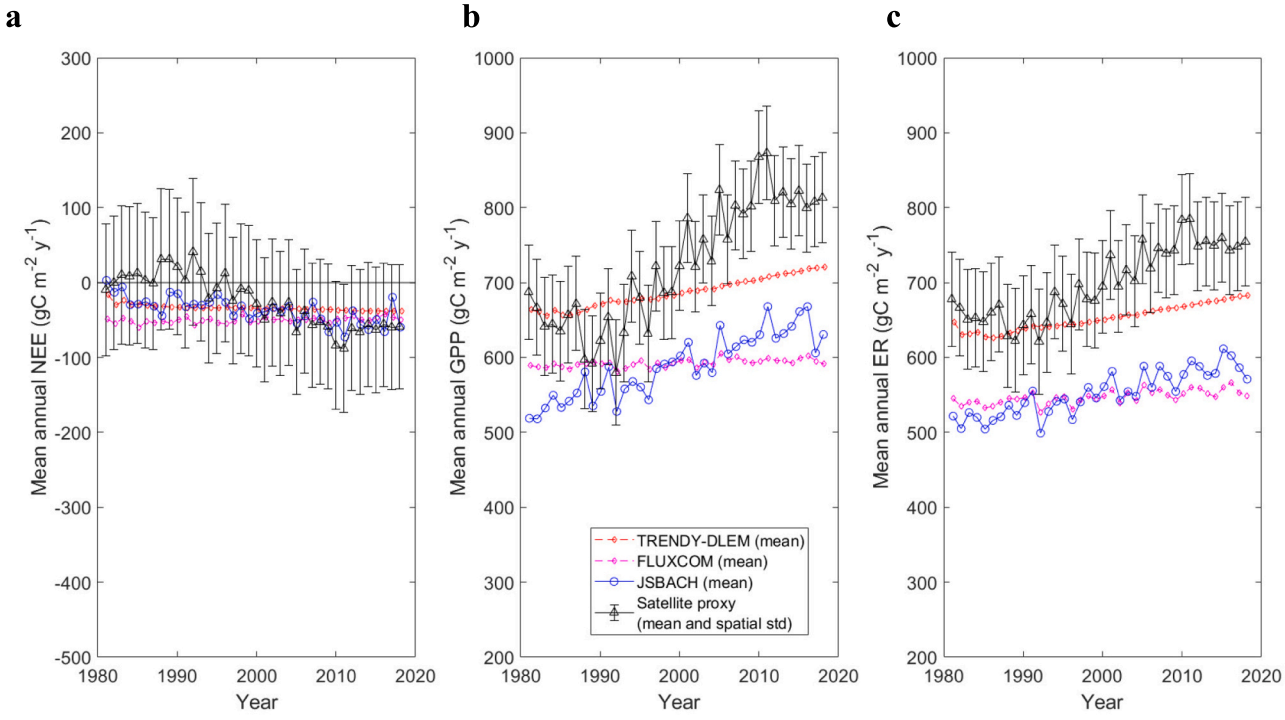

Fig. 11. Comparison of the satellite proxy with FLUXCOM, JSBACH ecosystem-climate model and TRENDY DLEM-S3 simulations. Average values across the circumpolar boreal forest are calculated for the yearly cumulative NEE, GPP and ER, and they are depicted for each data record for the period 1981–2018. The variabilities of annual estimates of NEE, GPP and ER are also shown for the satellite proxy (±standard deviation of all estimates from grid cells that represent the evergreen boreal forest zone).

the estimated uncertainty bounds suggest a small likelihood of circumpolar forests being a carbon source (Fig. 9a, Table 2). Results for the annual net carbon uptake show a significant increase during 1990–2010, but even a slight decrease during 2011–2018 driven by delayed spring snow melt (Figs. 1b, 9b). The assessed statistical uncertainty of the circumpolar GPP estimate obtained here for the period 2000–2018 is 7.5%, with ER the corresponding uncertainty is 8.1%, (Table 2). The results suggest that the strong increase in net CO_2 uptake during 1989–2018 is compensated largely by the co-incident increase in ecosystem respiratory releaseas of CO_2.

Author contributions

J.P. designed research; all authors contributed to the research, data analysis and writing of the paper.

CRediT authorship contribution statement

Jouni Pulliainen: Writing – review & editing, Writing – original draft, Visualization, Validation, Software, Methodology, Investigation, Formal analysis, Data curation, Conceptualization. **Mika Aurela:** Writing – review & editing, Investigation, Data curation, Conceptualization. **Tuula Aalto:** Writing – review & editing, Investigation, Data curation. **Kristin Böttcher:** Visualization, Investigation, Data curation. **Juval Cohen:** Writing – review & editing, Investigation, Data curation. **Chris Derksen:** Writing – review & editing, Data curation. **Martin Heimann:** Writing – review & editing, Data curation. **Manuel Helbig:** Writing – review & editing, Data curation. **Pasi Kolari:** Writing – review & editing, Data curation. **Anna Kontu:** Writing – review & editing, Conceptualization. **Alisa Krasnova:** Writing – review & editing, Data curation. **Samuli Launiainen:** Writing – review & editing, Data curation. **Juha Lemmetyinen:** Writing – review & editing, Data curation. **Hannakaisa Lindqvist:** Writing – review & editing, Visualization, Investigation, Data curation, Conceptualization. **Anders Lindroth:** Writing – review & editing, Data curation, Conceptualization. **Annalea Lohila:** Writing – review & editing, Data curation. **Kari Luojus:** Writing – review & editing, Data curation. **Ivan Mammarella:** Writing – review & editing, Data curation. **Tiina Markkanen:** Writing – review & editing, Investigation, Data curation. **Elma Nevala:** Writing – review & editing, Data curation. **Steffen Noe:** Writing – review & editing, Data curation. **Matthias Peichl:** Writing – review & editing, Data curation. **Jukka Pumpanen:** Writing – review & editing, Data curation. **Kimmo Rautiainen:** Writing – review & editing, Data curation. **Miia Salminen:** Writing – review & editing, Data curation. **Oliver Sonnentag:** Writing – review & editing, Investigation, Data curation, Conceptualization. **Matias Takala:** Writing – review & editing, Data curation. **Tea Thum:** Writing – review & editing, Data curation. **Timo Vesala:** Writing – review & editing, Funding acquisition, Data curation, Conceptualization. **Patrik Vestin:** Writing – review & editing, Data curation.

Declaration of competing interest

The authors declare that they have no known competing financial interests or personal relationships that could have appeared to influence the work reported in this paper.

Data availability

Data will be made available on request.

Acknowledgements

This work is supported by the Atmosphere and Climate Competence Center (Research Council of Finland); ICOS-Finland funded by University of Helsinki; E2S research infrastructure (Research Council of Finland); Research Council of Finland no. 350184 (WINMET); Research Council of Finland no. 330165 (RESEMON);

ESA-Metheo 4000125046/18/I-NB; EU-H2020 Grant 958927 (COCO2); EU-HORIZON grant no. 101081395 (EYE-CLIMA), no. 101056921 (GreenFeedBack); ESA-CryoBioLinks (4000135793/21/I-DT-lr); Estonian Research Council Grant PRG 1674; Estonian Ministry of Sciences projects (P180021, P180274, P200196); Estonian Research Infrastructures Roadmap Project “Estonian Environmental Observatory”; EU-H2020 Grant 871115; ACTRIS IMP; ERA-PLANET Grant 689443.

Appendix A. Supplementary data

Supplementary data to this article can be found online at https://doi.org/10.1016/j.rse.2024.114376.

References

Aurela, M., Lohila, A., Tuovinen, J.-P., Hatakka, J., Penttilä, P., Laurila, T., 2015. Carbon dioxide and energy flux measurements in four northern-boreal ecosystems at Pallas. Boreal Environ. Res. 20, 455–473.

Barr, A., Black, T., McCaughey, J., 2009. In: Noormets, A. (Ed.), Phenology of Ecosystem Processes. Springer, New York, pp. 3–34.

Bontemps, S., et al., 2011. GLOBCOVER: products Descrition and validation report. European Space Agency (ESRIN, Italy. Report 2.2).

Bradshaw, C.J.A., Warkentin, I.G., 2015. Global estimates of boreal forest carbon stocks and flux. Glob. Planet. Chang. 128, 24–30. https://doi.org/10.1016/j.gloplacha.2015.02.004.

Byrne, B., Liu, J., Yi, Y., et al., 2022. Multi-year observations reveal a larger than expected autumn respiration signal across Northeast Eurasia. Biogeosciences 19, 4779–4799. https://doi.org/10.5194/bg-19-4779-2022.

Chapin, F.S., Woodwell, G.M., Randerson, J.T., et al., 2006. Reconciling carbon-cycle concepts, terminology, and methods. Ecosystems 9, 1041–1050. https://doi.org/10.1007/s10021-005-0105-7.

Chi, J., Zhao, P., Klosterhalfen, A., et al., 2021. Forest floor fluxes drive differences in the carbon balance of contrasting boreal forest stands. Agric. For. Meteor. 306, 108454 https://doi.org/10.1016/j.agrformet.2021.108454.

Duveiller, G., Filipponi, F., Walther, S., Köhler, P., Frankenberg, C., Guanter, L., Cescatti, A., 2020. A spatially downscaled sun-induced fluorescence global product for enhanced monitoring of vegetation productivity. Earth Syst. Sci. Data 12, 1101–1116. https://doi.org/10.5194/essd-12-1101-2020.

El-Amine, M., Roy, A., Koebsch, F., et al., 2022. What explains the year-to-year variation in growing season timing of boreal black spruce forests? Agric. For. Meteorol. 324, 109113 https://doi.org/10.1016/j.agrformet.2022.109113.

Ensminger, I., Sveshnikov, D., Campbell, D.A., Funk, C., Jansson, S., Lloyd, J., Shibistova, O., Öquist, G., 2004. Intermittent low temperatures constrain spring recovery of photosynthesis in boreal scots pine forests. Glob. Chang. Biol. 10, 995–1008. https://doi.org/10.1111/j.1365-2486.2004.00781.x.

Fisher, R., Koven, C.D., Anderegg, W.L., et al., 2018. Vegetation demographics in earth system models: a review of progress and priorities. Glob. Chang. Biol. 24, 35–54. https://doi.org/10.1111/gcb.13910.

Foster, A.C., Wang, J.A., Frostet, G.V., et al., 2022. Disturbances in north American boreal forest and Arctic tundra: impacts, interactions, and responses. Environ. Res. Lett. 17, 113001 https://doi.org/10.1088/1748-9326/ac98d7.

Friedlingstein, P., Jones, M.W., Michael O'Sullivan, M., et al., 2022. Global carbon budget 2021. Earth Syst. Sci. Data 14, 1917–2005. https://doi.org/10.5194/essd-14-1917-2022.

Frolking, S., Goulden, M.L., Wofsy, S.C., Fan, S., Sutton, D.J., Munger, J.W., Bazzaz, A. M., Daube, B.C., Crill, P.M., Aber, J.D., Band, L.E., Wang, X., Savage, K., Moore, T., Harris, R.C., 1996. Modelling temporal variability in the carbon balance of a spruce/moss boreal forest. Glob. Chang. Biol. 2, 343–366. https://doi.org/10.1111/j.1365-2486.1996.tb00086.x.

Gamon, J.A., Huemmrich, K.F., Wong, C.Y.S., Ensminger, I., Garrity, S., Hollinger, D.Y., Noormets, A., Penuelas, J., 2016. A remotely sensed pigment index reveals photosynthetic phenology in evergreen conifers. Proc. Natl. Acad. Sci. 113, 13087–13092. https://doi.org/10.1073/pnas.1606162113.

Goulden, M.L., Wofsy, S.C., Harden, J.W., Trumbore, S.E., Crill, P.M., Gower, S.T., Fries, T., Daube, B.C., Fan, S., Sutton, D.J., Bazzaz, A., Munger, J.W., 1998. Sensitivity of boreal forest carbon balance to soil thaw. Science 279, 214–217. https://doi.org/10.1126/science.279.5348.214.

Guanter, L., Bacour, C., Schneider, A., et al., 2021. The TROPOSIF global sun-induced fluorescence dataset from the sentinel-5P TROPOMI mission. Earth Syst. Sci. Data 13, 5423–5440. https://doi.org/10.5194/essd-13-5423-2021.

Harris, I., Osborn, T.J., Lister, D.H., 2014. Updated high-resolution grids of monthly climatic observations - the CRU TS3.10 dataset. Int. J. Climatol. 34, 623–642. https://doi.org/10.1002/joc.3711.

Helbig, M., Chasmer, L., Desai, A., Kljun, N., Quinton, W., Sonnentag, O., 2017. Direct and indirect climate change effects on carbon dioxide fluxes in a thawing boreal forest–wetland landscape. Glob. Chang. Biol. 23, 3231–3324. https://doi.org/10.1111/gcb.13638.

Hollinger, D.Y., Goltz, S.M., Davidson, E.A., Lee, J.T., Tu, K., Valentine, H.T., 1999. Seasonal patterns and environmental control of carbon dioxide and water vapour

exchange in an ecotonal boreal forest. Glob. Chang. Biol. 5, 891–902. https://doi.org/10.1046/j.1365-2486.1999.00281.x.
Huntzinger, D.N., Post, W.M., Wei, Y., Michalaket, A.M., et al., 2012. North American carbon program (NACP) regional interim synthesis: terrestrial biosphere model intercomparison. Ecol. Model. 232, 144–157. https://doi.org/10.1016/j.ecolmodel.2012.02.004.
Jiang, Z., Heute, A.R., Didan, K., Miura, T., 2008. Development of a two-band enhanced vegetation index without a blue band. Remote Sens. Environ. 112, 3833–3845. https://doi.org/10.1016/j.rse.2008.06.006.
Jocher, G., Löfvenius, M., De Simon, G., et al., 2017. Apparent winter CO2 uptake by a boreal forest due to decoupling. Agric. For. Meteor. 232, 23–34. https://iranarze.ir/storage/uploads/2016/10/dx.doi.org/10.1016/j.agrformet.2016.08.002.
Jung, M., Schwalm, C., Migliavacca, M., et al., 2020. Scaling carbon fluxes from eddy covariance sites to globe: synthesis and evaluation of the FLUXCOM approach. Biogeosciences 17, 1343–1365. https://doi.org/10.5194/bg-17-1343-2020.
Kim, Y., Kimball, J.S., McDonald, K.S., Glassy, J., 2011. Developing a global data record of daily landscape freeze/thaw status using satellite passive microwave remote sensing. IEEE Trans. Geosci. Remote Sens. 49, 949–960. https://doi.org/10.1109/TGRS.2010.2070515.
Kim, Y., Kimball, J.S., Glassy, J., Du, J., 2017. An extended global earth system data record on daily landscape freeze–thaw status determined from satellite passive microwave remote sensing. Earth Syst. Sci. Data 9, 133–147. https://doi.org/10.5194/essd-9-133-2017.
Kimball, J.S., McDonald, K.C., Running, S.W., Frolking, S.E., 2004. Satellite radar remote sensing of seasonal growing seasons for boreal and subalpine evergreen forests. Remote Sens. Environ. 90, 243–258. https://doi.org/10.1016/j.rse.2004.01.002.
Krasnova, A., Mander, Ü., Noe, S.M., Uri, V., Krasnov, D., Soosaar, K., 2022. Hemiboreal forests' CO2 fluxes response to the European 2018 heatwave. Agric. For. Meteorol. 323, 109042 https://doi.org/10.1016/j.agrformet.2022.109042.
Lagergren, F., Lindroth, A., Dellwik, E., et al., 2008. Biophysical controls on CO2 fluxes of three northern forests based on long-term eddy covariance data. Tellus 60B, 143–152. https://doi.org/10.1111/j.1600-0889.2006.00324.x.
Lasslop, G., Migliavacca, M., Bohrer, G., et al., 2012. On the choice of the driving temperature for eddy-covariance carbon dioxide flux partitioning. Biogeosciences 9, 5243–5259. https://doi.org/10.5194/bg-9-5243-2012.
Launiainen, S., Katul, G.G., Leppä, K., Kolari, P., Aslan, T., Grönholm, T., Korhonen, L., Mammarella, I., Vesala, T., 2022. Does growing atmospheric CO2 explain increasing carbon sink in a boreal coniferous forest? Glob. Chang. Biol. 28, 2910–2929. https://doi.org/10.1111/gcb.16117.
Lloyd, J., Shibistova, O., Zolotoukhine, D., et al., 2002. Seasonal and annual variations in the photosynthetic productivity and carbon balance of a central Siberian pine forest. Tellus 54B, 590–610. https://doi.org/10.3402/tellusb.v54i5.16689.
López-Blanco, E., Exbrayat, J.-F., Lund, M., Christensen, T.R., Tamstorf, M.P., Slevin, D., Hugelius, G., Bloom, A.A., Williams, M., 2019. Evaluation of terrestrial pan-Arctic carbon cycling using a data assimilation system. Earth Syst. Dynam. 10, 233–235. https://doi.org/10.5194/esd-10-233-2019.
Luojus, K., Pulliainen, J., Takala, M., et al., 2021. GlobSnow v3.0 northern hemisphere snow water equivalent dataset. Scientific Data 8, 163. https://doi.org/10.1038/s41597-021-00939-2.
Melaas, E.K., Richardson, A.D., Friedl, M.A., Dragoni, D., Gough, C.M., Herbst, M., Montagnani, L., Moors, E., 2013. Using FLUXNET data to improve models of springtime vegetation activity onset in forest ecosystems. Agric. For. Meteorol. 171–172, 46–56. https://doi.org/10.1016/j.agrformet.2012.11.018.
Melser, R., Coops, N., Derksen, C., 2024. Characterizing satellite-derived freeze/thaw regimes through spatial and temporal clustering for the identification of growing season constraints on vegetation productivity. Remote Sens. Environ. https://doi.org/10.1016/j.rse.2024.114210.
Milyukova, I., Kolle, O., Varlagin, A., Vygodskaya, N., Schulze, E.-D., Lloyd, J., 2002. Carbon balance of a southern taiga spruce stand in European Russia. Tellus 54B, 429–442. https://doi.org/10.3402/tellusb.v54i5.16679.
Monson, R., Sparks, J., Rosenstiel, T., Scott-Denton, L., Huxman, T., Harley, P., Turnipseed, A., Burns, S., Backlund, B., Hu, J., 2005. Climatic influences on net ecosystem CO2 exchange during the transition from wintertime carbon source to springtime carbon sink in a high-elevation, subalpine forest. Oecologia 146, 130–147. https://doi.org/10.1007/s00442-005-0169-2.
Pallandt, M., Kumar, J., Mauritz, M., Schuur, E., Virkkala, A.-M., Celis, G., Hoffman, F., Göckede, M., 2022. Representativiness assessment of the pan-Arctic eddy covariance site network and optimized future enhancements. Biogeosciences 19, 559–583. https://doi.org/10.5194/bg-19-559-2022.
Pan, Y.D., Birdsey, R.A., Fang, J., et al., 2011. A large and persistent carbon sink in the world's forests. Science 333, 988–993. https://doi.org/10.1126/science.1201609.
Piao, S., Ciais, P., Friedlingstein, P., et al., 2008. Net carbon dioxide losses of northern ecosystems in response to autumn warming. Nature 451, 49–52. https://doi.org/10.1038/nature06444.
Pierrat, Z., Nehemy, M.F., Roy, A., Magney, T., Parazoo, N.C., Laroque, C., Pappas, C., Sonnentag, O., Grossmann, K., Bowling, D.R., Seibt, U., Ramirez, A., Johnson, B., Helgason, W., Barr, A., Stutz, J., 2021. Tower-based remote sensing reveals mechanisms behind a two-phased spring transition in a mixed-species boreal Forest. Journal of geophysical research. Biogeosciences 126. https://doi.org/10.1029/2020JG006191 e2020JG006191.
Pierrat, Z., Magney, T., Parazoo, N.C., Grossmann, K., Bowling, D.R., Seibt, U., Johnson, B., Helgason, W., Barr, A., Bortnik, J., Norton, A., Maguire, A., Frankenberg, C., Stutz, J., 2022. Diurnal and seasonal dynamics of solar-induced chlorophyll fluorescence, vegetation indices, and gross primary productivity in the boreal Forest. Journal of geophysical research. Biogeosciences 127. https://doi.org/10.1029/2021JG006588 e2021JG006588.
Pulliainen, J., 2006. Mapping of snow water equivalent and snow depth in boreal and sub-arctic zones by assimilating space-borne microwave radiometer data and ground-based observations. Remote Sens. Environ. 101, 257–269. https://doi.org/10.1016/j.rse.2006.01.002.
Pulliainen, J., Aurela, M., Laurila, T., et al., 2017. Early snowmelt significantly enhances boreal springtime carbon uptake. Proc. Natl. Acad. Sci. USA 114, 11081–11086. https://doi.org/10.1073/pnas.1707889114.
Pulliainen, J., Luojus, K., Derksen, C., et al., 2020. Patterns and trends of northern hemisphere snow mass from 1980 to 2018. Nature 581, 294–298. https://doi.org/10.1038/s41586-020-2258-0.
Pulliainen, J., Luojus, K., Lemmetyinen, J., Takala, M., Derksen, C., Mudryk, L., 2021. Estimation of hemispheric snow mass evolution based on microwave radiometry. In: In 2021 IEEE Int. Geosci. And Remote Sens. Symp. IGARSS, Brussels, Belgium, pp. 612–613. https://doi.org/10.1109/IGARSS47720.2021.9553042.
Randazzo, N.A., Michalak, A.M., Miller, C.E., Miller, S.M., Shiga, Y.P., Fang, Y., 2021. Higher autumn temperatures lead to contrasting CO2 flux responses in boreal forests versus tundra and shrubland. Geophys. Res. Lett. 48 https://doi.org/10.1029/2021GL093843 e2021GL093843.
Rautiainen, K., Lemmetyeinen, J., Schwank, M., et al., 2014. Detection of soil freezing from L-band passive microwave observations. Remote Sens. Environ. 147, 206–218. https://doi.org/10.1016/j.rse.2014.03.007.
Reick, C.H., Raddatz, T., Brovkin, V., Gayler, V., 2013. Representation of natural and anthropogenic land cover change in MPI-ESM. J. Adv. Model. Earth Syst. 5, 459–482. https://doi.org/10.1002/jame.20022.
Richardson, A.D., Black, A., Ciais, P., et al., 2010. Influence of spring and autumn phenological transitions on forest ecosystem productivity. Philos. Trans. R. Soc. B 365, 3227–3246. https://doi.org/10.1098/rstb.2010.0102.
Running, S., Zhao, M., 2021. MODIS/Terra Gross Primary Productivity Gap-Filled 8-Day L4 Global 500m SIN Grid V061. NASA EOSDIS Land Processes DAAC. Accessed 2022-06-06. doi:https://doi.org/10.5067/MODIS/MOD17A2HGF.061.
Ryu, Y., Berry, J.A., Baldocchi, D.D., 2019. What is global photosynthesis? History, uncertainties and opportunities. Remote Sens. Environ. 223, 95–114. https://doi.org/10.1016/j.rse.2019.01.016.
Sitch, S., Friedlingstein, P., Gruber, N., et al., 2015. Recent trends and drivers of regional sources and sinks of carbon dioxide. Biogeosciences 12, 653–679. https://doi.org/10.5194/bg-12-653-2015.
Sonnentag, O., 2021. AmeriFlux BASE CA-SMC Smith Creek, Ver. 1-5, AmeriFlux AMP, (dataset). Doi:10.17190/AMF/1767830.
Sonnentag, O., Marsh, P., 2021. AmeriFlux BASE CA-HPC Havikpak Creek, Ver. 1-5, AmeriFlux AMP, (Dataset). doi:10.17190/AMF/1773392.
Suni, T., Berninger, F., Markkanen, T., Keronen, P., Rannik, Ü., Vesala, T., 2003. Interannual variability and timing of growing-season CO2 exchange in a boreal forest. J. Geophys. Res. 108, 4265. https://doi.org/10.1029/2002JD002381.
Takala, M., Pulliainen, J., Metsamaki, S.J., Koskinen, J.T., 2009. Detection of snowmelt using spaceborne microwave radiometer data in Eurasia from 1979 to 2007. IEEE Trans. Geosci. Remote Sens. 47, 2996–3007. https://doi.org/10.1109/TGRS.2009.2018442.
Takala, M., Luojus, K., Pulliainen, J., Derksen, C., Lemmetyinen, J., Kärnä, J.-P., Koskinen, J., Bojkov, B., 2011. Estimating northern hemisphere snow water equivalent for climate research through assimilation of space-borne radiometer data and ground-based measurements. Remote Sens. Environ. 115, 3517–3529. https://doi.org/10.1016/j.rse.2011.08.014.
Tanja, S., Berninger, F., Vesala, T., et al., 2003. Air temperature triggers the recovery of evergreen boreal forest photosynthesis in spring. Glob. Chang. Biol. 9, 1410–1426. https://doi.org/10.1046/j.1365-2486.2003.00597.x.
Teubner, I., Forkel, M., Camps-Valls, G., et al., 2019. A carbon sink-driven approach to estimate gross primary production from microwave satellite observations. Remote Sens. Environ. 229, 100–113. https://doi.org/10.1016/j.rse.2019.04.022.
Thum, T., Aalto, T., Aurela, M., et al., 2009. Spring initiation and autumn cessation of boreal coniferous forest CO2 exchange assessed by meteorological and biological variables. Tellus B 61, 701–717. https://doi.org/10.1111/j.1600-0889.2009.00441.x.
Tian, H., Chen, G., Lu, C., et al., 2015. North American terrestrial CO2 uptake largely offset by CH4 and N2O emissions: toward a full accounting of the greenhouse gas budget. Clim. Chang. 129, 413–426. https://doi.org/10.1007/s10584-014-1072-9.
Vermote, E., et al., 2018. NOAA climate data record (CDR) of normalized difference vegetation index (NDVI), version 5. NOAA National Centers for Environmental Information. https://doi.org/10.7289/V5ZG6QH9.
Vestin, P., Mölder, M., Klujn, N., et al., 2020. Impacts of clear-cutting of a boreal forest on carbon dioxide, methane and nitrous oxide fluxes. Forests 11, 961. https://doi.org/10.3390/f11090961.
Virkkala, A.-M., Aalto, J., Rogers, B., et al., 2021. Statistical upscaling of ecosystem CO2 fluxes across the terrestrial tundra and boreal domain: regional patterns and uncertainties. Glob. Chang. Biol. 27, 4040–4059. https://doi.org/10.1111/gcb.15659.
Vogg, G., Heim, R., Hansen, J., Schäfer, C., Beck, E., 1998. Frost hardening and photosynthetic performance of scots pine (Pinus sylvestris L.) needles. I. Seasonal changes in the photosynthetic apparatus and its function. Planta 204, 193–200. https://doi.org/10.1007/s004250050246.
Walther, S., Voigt, M., Thum, T., Gonsamo, A., Zhang, Y., Köhler, P., Jung, M., Varlagin, A., Guanter, L., 2016. Satellite chlorophyll fluorescence measurements reveal large-scale decoupling of photosynthesis and greenness dynamics in boreal evergreen forests. Glob. Chang. Biol. 22, 2979–2996. https://doi.org/10.1111/gcb.13200.
Wild, B., Teubner, I., Moesinger, L., Zotta, R.-M., Forkel, M., van der Schalie, R., Sitch, S., Dorigo, W., 2022. VODCA2GPP – a new, global, long-term (1988-2020) gross

primary production dataset from microwave remote sensing. Earth Syst. Sci. Data 14, 1063–1085. https://doi.org/10.5194/essd-14-1063-2022.

Xiao, J., Ollinger, S.V., Steve Frolking, S., et al., 2014. Data-driven diagnostics of terrestrial carbon dynamics over North America. Agric. For. Meteor. 197, 142–157. https://doi.org/10.1016/j.agrformet.2014.06.013.

Xiao, J., Chevallier, F., Gomez, C., et al., 2019. Remote sensing of terrestrial carbon cycle: a review of advances over 50 years. Remote Sens. Environ. 233, 111383 https://doi.org/10.1016/j.rse.2019.111383.

Yang, H., Ciais, P., Frappart, F., et al., 2023. Global increase in biomass carbon stock dominated by growth of northern youngforests over past decade. Nat. Geosci. 16, 886–892. https://doi.org/10.1038/s41561-023-01274-4.

Zhao, B., Zhuang, Q., Shurpali, N., et al., 2021. North American boreal forests are a large carbon source due to wildfires from 1986 to 2016. Sci. Rep. 11, 7723. https://doi.org/10.1038/s41598-021-87343-3.